Lensless single-shot dual-wavelength digital holography for industrial metrology

Shangguan, Huangcheng; Urbach, H. Paul; Kalkman, Jeroen

DOI
10.1364/AO.519491

Publication date
2024

Document Version
Final published version

Published in
Applied Optics

Research Article Vol. 63, No. 16 / 1 June 2024 / Applied Optics 4427

applied optics

Lensless single-shot dual-wavelength digital holography for industrial metrology

HUANGCHENG SHANGGUAN, H. PAUL URBACH, AND JEROEN KALKMAN*

Department of Imaging Physics, Delft University of Technology, Lorentzweg 1, 2628 CJ, Delft, The Netherlands
**j.kalkman@tudelft.nl*

Received 25 January 2024; revised 27 April 2024; accepted 8 May 2024; posted 9 May 2024; published 29 May 2024

We demonstrate lensless single-shot dual-wavelength digital holography for high-speed 3D imaging in industrial inspection. Single-shot measurement is realized by combining off-axis digital holography and spatial frequency multiplexing of the two wavelengths on the detector. The system has 9.1 μm lateral resolution and a 50 μm unambiguous depth range. We determine the theoretical accuracy of off-axis dual-wavelength phase reconstruction for the case of shot-noise-limited detection. Experimental results show good agreement with the proposed model. The system is applied to industrial metrology of calibrated test samples and chip manufacturing.

https://doi.org/10.1364/AO.519491

1. INTRODUCTION

Industrial inspection of manufactured components is critical in ensuring product quality and performance. In the measurement of component structure, e.g., analysis of surface defects, and assessment of dimensional accuracy and assembly quality, optical inspection plays a vital role [1–3]. Challenges in this field are obtaining high spatial resolution, large field of view, rapid measurement, and 3D imaging capability. 3D imaging extracts depth information thereby enabling the detection of defects that may be overlooked when relying solely on 2D images. Common optical 3D imaging methods [2] include stereo vision, fringe projection profilometry, and optical coherence tomography. Yet their limitation lies in their limited resolution, need for scanning in time, or the need for multiple cameras. In mass production industries, such as semiconductor production and assembly, high-speed imaging is important for real-time monitoring of product quality, which is challenging with current imaging modalities. Digital holography [4–7] is a technique that enables full-field depth-resolved single-shot measurement with a field of view and resolution comparable to classical microscopes, thereby meeting the demands of many industrial inspections.

Digital holography (DH) can simultaneously retrieve the amplitude and phase of the optical field and reconstruct the 3D shape of the object from it [8–10]. In industrial applications DH primarily operates in reflection mode where the phase change of non-transparent objects is caused by the height variation of the surface. Many studies [11–13] have shown the efficacy of DH in reconstructing various industrial components, including those that are reflective or matte, or have steep edges, demonstrating its robustness and wide applicability. Another notable advantage of DH is its ability of wavefront reconstruction, enabling numerical propagation for refocusing to any plane of interest. Unlike classical microscopes, DH does not rely on lenses for "imaging" [14], thereby avoiding lens aberrations, but also making the setup compact and circumventing cumbersome mechanical focusing operations.

A major limitation of the classical DH is that it cannot retrieve an unambiguous depth when the optical path difference is larger than the illumination wavelength due to the "2π ambiguity." This can be solved using phase unwrapping algorithms. However, this works well only for a gradual and continuous changing sample surface [15–18]. Dual-wavelength DH (DWDH) [19–21] alleviates the phase wrapping problem by employing measurements at two wavelengths and subtracting the phases of their fields to get the beat phase corresponding to the synthetic wavelength. The synthetic wavelength is larger than the illumination wavelength and defines the "new" unambiguous measurement range. The closer the wavelengths of the two lasers are, the larger the synthetic wavelength will be. For example, Abeywickrema *et al*. [22] achieved a centimeter-scale measurement range with an acousto-optic modulator by sequentially measuring holograms at two wavelengths. For high speed acquisition the holograms at the two wavelengths also can be measured in a single-shot measurement, by using spectral multiplexing with a Bayer mosaic color camera [23–25] or by combining an off-axis configuration with spatial frequency multiplexing [26], the latter of which is widely adopted due to better image resolution and more economical monochrome cameras. For instance, Fratz *et al*. [27,28] designed a multi-wavelength DH system with a synthetic wavelength ranging up to 1 mm that was successfully applied for detection in a precision turning plant. Piniard *et al*. [29] reported a dual-wavelength system for *in situ* real-time investigation of the melt pool morphology. Many papers [30–33] have also reported improvements to

off-axis-based DWDH to develop applications in different fields. However, all the aforementioned papers use lenses for imaging, and thus, the lensless imaging capability of DH, as well as the advantages it brings in making systems more compact, have not been fully exploited.

Even though the wavelength separation between the two wavelengths determines the unambiguous measurement range, the accuracy in determining the surface height depends on the accuracy of the phase estimation at the synthetic wavelength [34–36]. The phase estimation is influenced by noise from environmental vibrations, laser power fluctuations, and shot noise. Additionally, for rough surfaces, the diffuse scattering introduces additional phase noise and decoherence of the optical fields, further impacting phase estimation. Piniard *et al*. [37] investigated the impact of noise in DWDH; however, their study focused on the effect of surface roughness on phase measurements, in which case the scattering decorrelation noise was the dominant factor. A few studies [38–40] indicate that, after excluding environmental and sample factors, shot noise is the ultimate factor affecting phase accuracy in DH, and its impact on the phase measurement has been extensively examined, albeit limited to the single-wavelength scenario.

Realizing the large and steep height variations on object surfaces during industrial inspections and the need for fast, accurate, and large-depth-range 3D imaging for integrated circuits (IC) process control, we propose a high-phase-accuracy, single-shot DWDH system. The adoption of a lensless configuration makes the setup compact and easy to integrate into existing industrial equipment. We analyze the imaging field of view and spatial resolution in the lensless configuration and their limit factors. Additionally, we extend the single-wavelength DH shot-noise model proposed by Chen [39] to the DWDH scenario. Based on a theoretical analysis of our extended noise model and comparison with experimental results, we demonstrate the feasibility of our model and show that the shot-noise-limited phase sensitivity is approached. We show the successful application of single-shot large-depth-range imaging of IC micro-structures and chip tilt detection.

2. METHODS

A. Lensless Digital Holography Setup

The setup of the lensless single-shot DWDH is illustrated in Fig. 1(a). A He–Ne laser (HRS015B, Thorlabs) with wavelength $\lambda_1 = 633$ nm and a laser diode (CPS650F, Thorlabs) with wavelength $\lambda_2 = 637$ nm are used as light sources and yield a synthetic wavelength $\Lambda = \lambda_1\lambda_2/|\lambda_1 - \lambda_2| \approx 100$ μm. Both beams first pass through a beam expander to increase the beam size to cover the entire sample. The beam expander for λ_1 is composed of two positive lenses (LA1805-A and LA1509-A, Thorlabs) and a pinhole (P30K, Thorlabs) and for λ_2 is composed of two lenses (LA1131-A and LA1509-A, Thorlabs) and a pinhole (P25K, Thorlabs). The purpose of the pinhole is to filter out high-spatial-frequency noise from the laser output, producing a clean Gaussian-shaped illumination. The expanded beam for λ_i, with $i = 1, 2$, is then split into two fields with a cube beam splitter (BS013, Thorlabs). In one arm, the field illuminates the object, and its reflected field is redirected by a pellicle beam splitter (BP250, Thorlabs) and captured by the

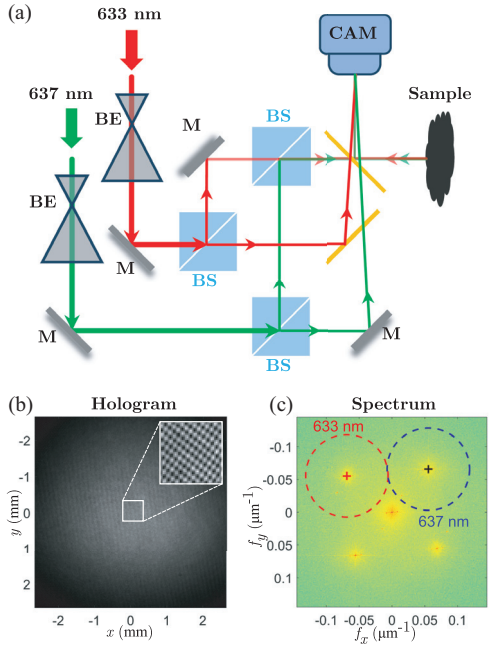

Fig. 1. (a) Schematic overview of the lensless single-shot DWDH setup. BE, beam expander; M, mirror; BS, beam splitter; CAM, camera. (b) An acquired dual-wavelength hologram. (c) The power spectrum of the hologram of (b).

camera; this is the object field O_i. The object field has an amplitude $|O_i|$ and phase φ_i. In the reference arm, the field R_i, reaches the camera after reflection by a mirror and transmission through the pellicle beam splitter. The interference of these two fields produces an interference pattern (hologram). The reference beam R_i is an inclined plane wave, with spatial frequencies $f_{x,i}$ and $f_{y,i}$ along the x and y directions, respectively. The subscript $i = 1, 2$ indicates the two wavelengths.

In our setup, the two illumination fields propagate coaxially to the sample along the direction of the optical axis while the two reference beams approach the camera at different angles giving rise to different spatial frequencies. Through variation of the incident angle, the interference fringes for λ_1 and λ_2 are orientated along the two diagonals of the sensor, leading to their spectra (Fourier transform of the hologram) to appear at a frequency axis orthogonal to the direction of their fringes. Positioned at an approximate distance of 70 mm from the sample holder, a monochrome 8-bit camera (MC124MG-SY-UB, XIMEA) with dimensions of 4112×3008 pixels and a pixel size $\Delta x = \Delta y = 3.45$ μm is employed. The numerical aperture (NA) for a lensless system is equal to the half open angle from the sample to the sensor, i.e., $\mathrm{NA} = \mathrm{W_{cam}}/2d$, where $\mathrm{W_{cam}}$ is the width of the camera sensor, and d is the distance between the object and camera. To accommodate the beam size, only 1536×1536 pixels of the sensor area (5.3×5.3 mm^2) were used in our measurements, resulting in an $\mathrm{NA} = 0.035$ and a field of view (FOV) of 28.09 mm^2. The exposure time for the hologram in our measurements was around 60 μs and varied depending on the samples to be measured. Because the two fields from the two wavelengths are not coherent with each other, the intensity of the dual-wavelength hologram I_{DW} captured by the camera is the sum of the two single-wavelength holograms [30]:

$$
\begin{aligned}
I_{\mathrm{DW}} &= |O_1|^2 + |R_1|^2 + O_1 R_1^* + O_1^* R_1 \\
&\quad + |O_2|^2 + |R_2|^2 + O_2 R_2^* + O_2^* R_2 \\
&= |O_1|^2 + |R_1|^2 + |O_2|^2 + |R_2|^2 \\
&\quad + 2|O_1||R_1|\cos(\varphi_1 - f_{x,1}x - f_{y,1}y) \\
&\quad + 2|O_2||R_2|\cos(\varphi_2 - f_{x,2}x - f_{y,2}y), \qquad (1)
\end{aligned}
$$

where all fields are functions of spatial coordinates x and y. Figures 1(b) and 1(c) show an example of an acquired hologram and its corresponding spectrum. The inset in Fig. 1(b) illustrates a chessboard-like interference pattern caused by the cross-overlapping of the two interference fringes. In contrast, Fig. 1(c) presents well-separated spectra, thanks to the different spatial frequencies carried by the two reference beams. The cross marker indicates the center position of the sideband ($O_i R_i^*$). According to Fourier optics, the cutoff frequency of the sideband is $f_{c,i} = \mathrm{NA}/\lambda_i = \mathrm{W}_{\mathrm{cam}}/(2\lambda_i d)$. The circles indicate the spectral range that will be truncated during the subsequent reconstruction and is set to be slightly broader than the bandwidth of the sideband $f_{c,i}$.

B. Object Field Reconstruction

The Fourier-transform-based filtering algorithm is an efficient and straightforward reconstruction method for off-axis DH and can also be applied to DWDH. First, the hologram is Fourier transformed to determine its power spectrum, as depicted in Fig. 1(c), where the spectra of the real/virtual image terms for the two wavelengths are cross-diagonally distributed due to off-axis illumination. Second, two band-pass masks are created to selectively filter the spectra of the two fields ($O_i R_i^*$). The location of the mask center is determined by the coordinates of the maximum value of the sideband. The selection of the mask radius, as described in the previous section, needs to be larger than the cutoff frequency $f_{c,i}$. The cutoff frequency $f_{c,i}$ can only be approximated at first, by reasonably estimating the distance between sample and camera d. After obtaining the precise distance by refocusing, $f_{c,i}$ can be updated once again. We further multiply the estimated mask radius $f_{c,i}$ by 1.1 to avoid loss of spatial resolution. Third, the filtered spectrum undergoes an inverse Fourier transform, followed by compensation for the phase slope of the reference field through multiplication with a digitally generated reference beam R_i^{dig} based on the centroid of the off-axis term [29] to determine the spatial frequency of R_i^{dig}. Finally, we perform a linear phase fitting and subtraction to reduce the phase residue. At this point, the object field, which is the field diffracted from the object onto the detector, is obtained. The undiffracted field in the sample plane is obtained through back propagation using the angular spectrum method [41]. The propagation distance to the sample is determined by searching for the distance at which the image edges are sharpest [11]. It is worth pointing out that imperfection in laser alignment or inaccuracy in slope phase compensation may result in a slight offset between the two on-focus images. In such cases, image registration is recommended. Finally, the phase map φ_i is retrieved by extracting the imaginary and real parts of the resulting complex field and then calculating the arctangent of the ratio. The process for phase retrieval at the two wavelengths in off-axis dual-wavelength digital holography can be summarized as [30]

$$
\varphi_i = \mathrm{angle}\left(\mathcal{F}^{-1}\{\mathcal{F}\{I_{\mathrm{DW}}\} \cdot \mathrm{Mask}_i\} \cdot R_i^{\mathrm{dig}}\right). \qquad (2)
$$

Note that both phase maps φ_i are wrapped, which prevents extracting the height map of the sample correctly from each individual phase map. This issue can be resolved by calculating the so-called beat phase Φ in dual-wavelength digital holography as [30]

$$
\Phi = \varphi_1 - \varphi_2 = 2\pi\,\mathrm{OPL}\left(\frac{1}{\lambda_1} - \frac{1}{\lambda_2}\right) = 2\pi\frac{\mathrm{OPL}}{\Lambda}, \qquad (3)
$$

where OPL denotes the optical path length, which is twice the height map of the sample due to the setup working in reflection mode. Examination of Eq. (3) reveals that the phase Φ is wrapped only when $\mathrm{OPL} > \Lambda$. In contrast, for single-wavelength DH, the phase φ_i becomes wrapped once $\mathrm{OPL} > \lambda_i$, which explains why DWDH can unambiguously measure objects with substantial height differences without the need for phase unwrapping algorithms. The data processing time for the whole process of beat phase estimation is around 1.2 s for a 1536 × 1536 pixel hologram (using an Intel Xeon W-2223 CPU at 3.60 GHz). Obviously, the closer the two wavelengths, the larger the synthetic wavelength Λ, allowing for larger height difference measurement. However, as the two wavelengths draw closer, the impact of laser source bandwidth and wavelength drift becomes more significant. Since the height accuracy scales with Λ in Eq. (3), a larger synthetic wavelength at the same single-wavelength phase sensitivity φ_i leads to a reduction in height estimation accuracy. Hence, it is of paramount importance to achieve the highest phase sensitivity possible.

C. Theoretical Accuracy of DWDH Phase Estimation

The accuracy of phase measurement defines the height accuracy and can be quantified by the standard deviation of the phase reconstruction $\sigma(\varphi)$. This metric not only reflects the minimal detectable phase change but also describes the spread in phase measurements over time. In practice, surface roughness, technical noises, and environment will influence the accuracy of phase measurement [37–40]. For a polished surface, the impact of roughness could be irrelevant compared to other noise sources [37,40]. Maintaining stable experimental conditions and using a high-performance camera can effectively decrease many types of noise, such as dark-current and background noise. However, shot noise is the ultimate limiting factor and sets a baseline for the phase accuracy [38,39]. Chen *et al.* [39] theoretically studied the phase sensitivity for single-wavelength off-axis DH and derived an analytical expression for the best achievable phase accuracy estimation under shot-noise-limited detection:

$$
\sigma_\varphi = \sqrt{\frac{|O|^2 + |R|^2}{2g|O|^2|R|^2}\frac{S}{MN}}, \qquad (4)
$$

where the intensities are measured in photoelectron counts on the camera, "g" is the camera gain, and S/MN denotes the ratio of the filter area S to the entire Fourier area MN. The ratio of the DC term of the hologram over the amplitude of the interference is the reciprocal of the fringe visibility. It is worth noting that the accuracy $\sigma(\varphi_i)$ is a function of x and y as a result of the non-uniformity of the reference and sample field. The camera gain "g," with unit of e^-/ADU, is calibrated using the mean-variance fitting method [42], serving as the conversion factor between the number of photoelectrons and the analog-to-digital unit (ADU) reading of the camera. A higher "g" leads to improved phase accuracy (decreasing phase standard deviation). This is consistent with physical intuition: with a larger camera gain at the same camera readout, a pixel contains more photoelectrons; therefore, the impact of shot noise, which follows a Poisson distribution, on the signal decreases. The calibrated gain of the camera we used is $g = 9.6 \pm 0.15$.

We apply the phase accuracy model Chen *et al.* [39] to off-axis DWDH. First, due to the non-coherence of the two independent laser sources and the linear detection efficiency, the dual-wavelength hologram of Eq. (1) can be considered as a superposition of two individual single-wavelength holograms. Second, as previously discussed, the respective amplitudes $|O_i|$ for each wavelength can be determined utilizing different filters via Fourier filtering. Therefore, following similar derivation steps, we find that the phase accuracy σ_{φ_i} reconstructed from a dual-wavelength hologram under the condition of shot-noise-limited detection is

$$\sigma_{\varphi_i} = \sqrt{\frac{|O_1|^2 + |R_1|^2 + |O_2|^2 + |R_2|^2}{2g|O_i|^2|R_i|^2}\frac{S}{MN}}. \tag{5}$$

This expression shares a close resemblance with Eq. (4). The difference lies in the DC term: in the dual-wavelength case, the DC term is the summation of the two DC terms from the two individual single wavelengths. To avoid detector saturation, the maximum value of $|O_i||R_i|$ in dual-wavelength needs to be smaller than in the single-wavelength case. Consequently, when using the same hardware and reconstruction algorithm, a comparison of Eqs. (4) and (5) suggests that, even if the phase measurement accuracy at an individual wavelength is the focus of interest, the phase accuracy obtained from a dual-wavelength hologram is inferior to that from a single-wavelength hologram. For DWDH with equal power in the two wavelengths, a total power of the illumination equal to that for the single-wavelength case, and a perfectly balanced interferometer, the phase accuracy at individual wavelengths is a factor $\sqrt{2}$ worse than the result from a single-wavelength DH measurement.

For the beat phase Φ, which is given by the subtraction of two independent phase maps, as expressed in Eq. (3), its variance equals the sum of the variances of the other two phases, i.e.,

$$\begin{aligned}\sigma_\Phi^2 &= \sigma_{\varphi_1}^2 + \sigma_{\varphi_2}^2 \\ &= \frac{|O_1|^2 + |R_1|^2 + |O_2|^2 + |R_2|^2}{2g}\frac{S}{MN} \\ &\quad \times \left[\frac{1}{|O_1|^2|R_1|^2} + \frac{1}{|O_2|^2|R_2|^2}\right].\end{aligned} \tag{6}$$

This can be considered the shot-noise-limited phase accuracy for DWDH and can be converted to height accuracy via Eq. (3). Equations (5) and (6) make it possible to quantify and evaluate the phase accuracy of a DWDH setup, solely from one hologram.

3. RESULTS

A. Lateral Resolution and Field of View

In conventional optical microscopy, there is generally a trade-off between the lateral field of view (FOV) and image resolution as the objective lens and tube lens are matched for a minimal aberration. While a high-NA objective lens can enhance the lateral resolution, it comes at the expense of a smaller lateral FOV, and vice versa. In a lensless DH setup with plane wave illumination, the imaging FOV is equal to the sensor size, and the lateral resolution is determined by both the NA of the system and the pixel size of the sensor Δx. According to the Abbe criteria, the theoretical resolution can be calculated using the formula $r_A = \lambda/2\mathrm{NA}$. Decreasing the distance from the sample to the sensor or increasing the sensor size can increase the NA of the system and improve resolution. However, it ultimately is limited by the finite pixel size, because the image is discretely sampled by the sensor in lensless DH. This usually does not pose a big problem in classical microscopes, because in magnified images the point spread function is wider than the pixel size.

The experimentally achievable resolution and FOV were determined by imaging a USAF resolution target; see Fig. 2. Figures 2(a) and 2(b) show the acquired 5×5 mm^2 hologram and the corresponding power spectrum, respectively. The width of the spectrum, also referred to as the sensor bandwidth, depends on the pixel size Δx and is equal to $1/\Delta x$. According to the Nyquist theorem, only signals with a spatial frequency within the sensor bandwidth can be accurately sampled and retrieved. Since the spectra of the fields $O_i R_i^*$ and their complex conjugates are symmetrically distributed and have the same bandwidth, the optimal spectrum arrangement in DWDH should be a diagonal distribution with the two wavelengths along different diagonals, as shown in Fig. 2(b). The dashed circle in the figure indicates the bandwidth of the sideband, which is smaller than the sensor bandwidth, leading to the achievable resolution given by the Abbe diffraction limit. During the data processing, the distance from the sample to the sensor was found to be 76.11 mm. Consequently, $r_A \approx 9.1$ μm was the best achievable DWDH resolution, as the resolutions for the two wavelengths are almost equal.

The reconstructed intensities for λ_1 and λ_2 are shown in Figs. 2(c) and 2(d), respectively. The insets display zoomed-in images of the red dashed box area, from which we can see that the smallest distinguishable pattern is element 5-5, which has 50.8 line pairs per millimeter. Also note that the FOV of the images is 5×5 mm^2, the same dimensions as the hologram in Fig. 2(a). However, only part of the FOV is useful as the beam intensity is diminished at the edges. Figures 2(e) and 2(f) show the respective phase maps of the zoomed-in image for λ_1 and λ_2, respectively. Figure 2(g) shows both the intensity and phase profiles of element 5-5 along the dashed line in Figs. 2(c)–2(f). We can observe that this set of patterns just can be resolved for both intensity and phase. Therefore, it can be concluded that

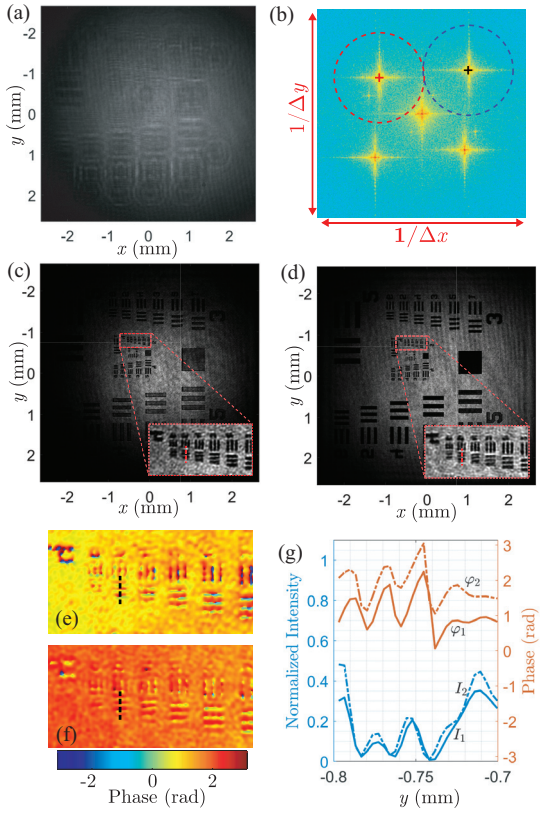

Fig. 2. DWDH measurement on USAF resolution target. (a) The acquired dual-wavelength hologram. (b) The corresponding power spectrum. The width is equal to $1/\Delta x$. (c), (d) Reconstructed intensity maps for λ_1 and λ_2, where the inset represents the zoomed-in image of the selected areas. (e), (f) The respective phase map of the selected areas in (c) and (d). (g) Intensity and phase profile curves of element 5-5 of the USAF target.

the spatial resolution of the setup is better than 9.84 μm, a value close to the theoretical resolution of $r_A \approx 9.1$ μm.

B. Phase Accuracy

The phase measurement accuracy for DWDH was experimentally quantified and compared with the theoretical model. A silver mirror was used as the object to avoid the influence of the scattering decorrelation noise on the phase that stems from the surface roughness. The experimental method for measuring the phase accuracy is as follows: first, we took a series of holograms at 40 ms intervals during 10 s. Second, the phase maps from each hologram were reconstructed separately for the two wavelengths and the synthetic wavelength by using Eqs. (2) and (3), that is, φ_1, φ_2, and Φ. Finally, the standard deviation σ_{exp} of the phase variation at every location was calculated from the time series. Figure 3(a) shows the three phase maps for λ_1, λ_2, and Λ reconstructed from one of the captured holograms. The phases are constant for the mirror object. Figure 3(b) shows the variation of the phase at one point (marked with a red cross) in Fig. 3(a) on each reconstruction, and the statistical distribution is shown in the histogram. As can be seen, due to noise in the experiment, there are temporal fluctuations in the phase. We can obtain the

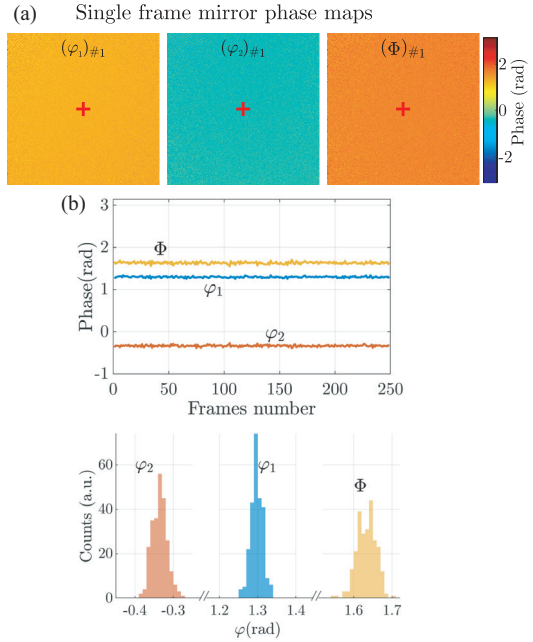

Fig. 3. (a) DWDH reconstructed phase maps of a mirror sample for λ_1, λ_2, and Λ. (b) The phase change over time for the three phases at the selected point in (a). The histogram on the right shows the corresponding statistical distribution.

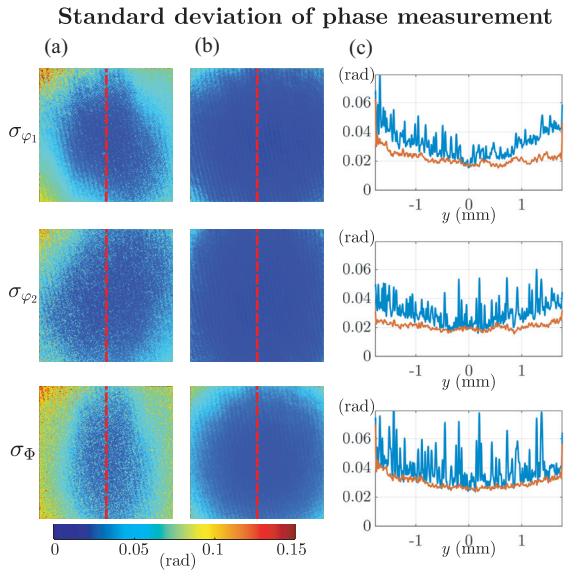

Fig. 4. (a) Experimental and (b) theoretical DWDH phase accuracy comparison for λ_1, λ_2, and Λ. (c) Comparison along the red lines in (a) and (b), where the blue line is the experimental data and the red line is the theoretical prediction.

phase measurement accuracies σ_{exp} at the indicated point, which are 15.8, 19.7, and 24.7 mrad for λ_1, λ_2, and Λ, respectively.

The spatially resolved phase measurement accuracy maps are illustrated in Fig. 4. Figure 4(a) shows the experimental phase accuracy for λ_1, λ_2, and Λ and Fig. 4(b) shows the theoretical phase accuracy calculated with Eqs. (5) and (6). All parameters required to obtain the theoretical accuracy can be computed from a single captured hologram. A quantitative comparison

between the theoretical and experimental accuracy is presented in Fig. 4(c); each plot corresponds to the comparison along the red dashed lines in Figs. 4(a) and 4(b). From Fig. 4(c), it can be seen that higher phase accuracy appears at the center of the detector area for both the experimental and theoretical accuracy. This characteristic can be explained by the Gaussian illumination profile, which results in a higher intensity (more photons) at the center and thus less noise. Furthermore, the comparison reveals that the experimental accuracy is basically lower bounded by the theoretical accuracy. The theoretical accuracy is based on shot noise only; however, the severe fluctuations observed in the experimental results imply that other factors such as readout noise, pixel inconsistency, and source instability also affect our measurements to some extent.

C. Application to Industrial Inspection

Several experiments were conducted to demonstrate the applicability of our setup for industrial inspection. Figure 5 shows quantitative 3D reconstruction of a metal workpiece (manufactured by Rubert & Co Ltd, product type 515), which consists of six engraved grooves on its surface (with depths of 1, 5, 10, 50, 100, 1000 μm). Figure 5(a) is the acquired dual-wavelength hologram, which is a superposition of two interference patterns. The inset in Fig. 5(a) depicts the power spectrum density distribution of the hologram. The spectrum shows that the spectra for

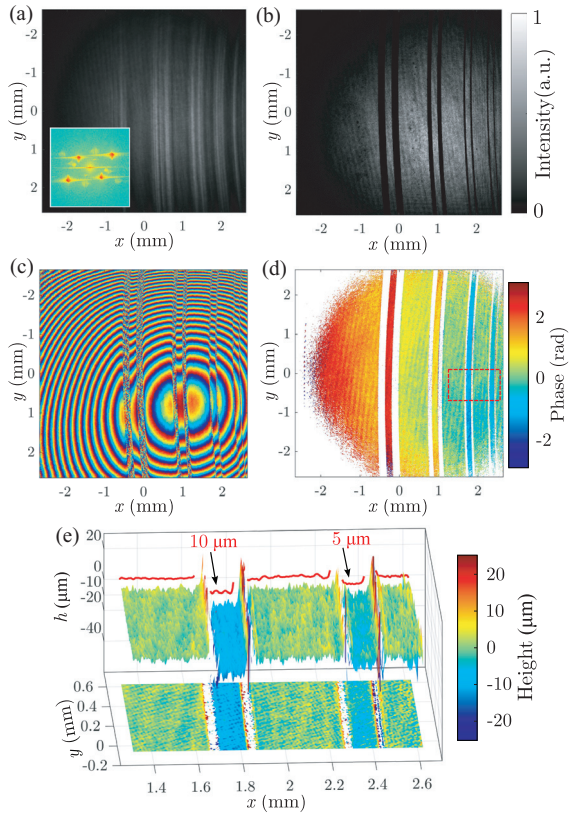

Fig. 5. DWDH measurement on a metal workpiece. (a) The obtained dual-wavelength hologram, where the inset shows its spectrum. (b), (c) Reconstructed intensity and wrapped phase for λ_1. (d) Beat phase map computed by Eq. (3) after tilt compensation and ignoring low-intensity areas. (e) 3D topography map of the selected area in (d).

λ_1 and λ_2 are diagonally distributed and well separated. Figures 5(b) and 5(c) show the reconstructed intensity and phase map for λ_1 (the result for λ_2 has a similar appearance). The phase map, Fig. 5(c), displays a wrapped phase according to spherical waves, which is caused by the slight concavity on the workpiece surface. Nevertheless, the presence of the grooves is still discernible, as the groove depth introduces additional phase delays, resulting in discontinuities in the phase distribution around the groove edges.

The beat phase map Φ, computed via Eq. (3) and after subtraction of a linear phase tilt, is illustrated in Fig. 5(d). It is evident from the figure that the issue of phase wrapping has been significantly alleviated, and that the grooves are well visible due to their difference in phase value with respect to the surface. The phase values in regions with insufficient intensity have been removed and replaced with NAN (not a number). This is necessary, as calculating the phase in these areas results in an ill-defined phase due to the denominator of the arctangent being zero or close to zero. These regions occur around the periphery of the image and on either side of the grooves. The former is attributed to the non-uniform illumination of the Gaussian beam, while the latter is because the grooves have very vertical side walls, making it challenging to obtain reflective light from these areas. Figure 5(e) demonstrates a 3D topography map of the region highlighted in red in Fig. 5(d) where the phase has been converted to height distribution and the linear phase has been subtracted. The 3D map clearly distinguishes the presence of two grooves with nominal depths of 5 and 10 μm. The red line depicted in Fig. 5(e) denotes the projection of the reconstructed height distribution along the y-axis, confirming that the depths of the identified grooves are in line with the expected nominal values. The manufacturer stated nominal bottom width of the 10 μm groove measures 134 μm and that of the 5 μm measures 111 μm. These two dimensions measured from our results are 132.6 ± 3.9 and 119.4 ± 7.5 μm, respectively. Given that the discretization interval of the image equals the pixel size (3.45 μm), the deviation between the measurement and the nominal value is reasonable.

Figure 6 demonstrates the application of DWDH to industrial 3D chip inspection to determine the tilt of a die on a substrate. This tilt primarily results from the shrinkage and expansion of the glue solidification during the adhesive bonding process. The recorded hologram and its corresponding spectrum are illustrated in Fig. 6(a) and the inset therein. Figure 6(b) shows the reconstructed intensity at the surface of the chip, which is a superposition of the intensities for λ_1 and λ_2. While the intensity map provides many details about the chips, it fails to discern the presence of any tilt of the die. Furthermore, since the amount of tilt is minimal, the focus variance does not noticeably vary. However, the phase map clearly highlights this tilt as it appears in the form of distinctly increasing phase values. Figure 6(c) shows the height calculated from the two wrapped phases with the help of Eq. (3), wherein phases with excessively low intensities were omitted for better visibility. The tilt of the chip can be seen as the color variation from upper left to bottom right. After 3D plane fitting operation, the tilt angle θ relative to the xy plane is quantified as 0.38 ± 0.006 deg.

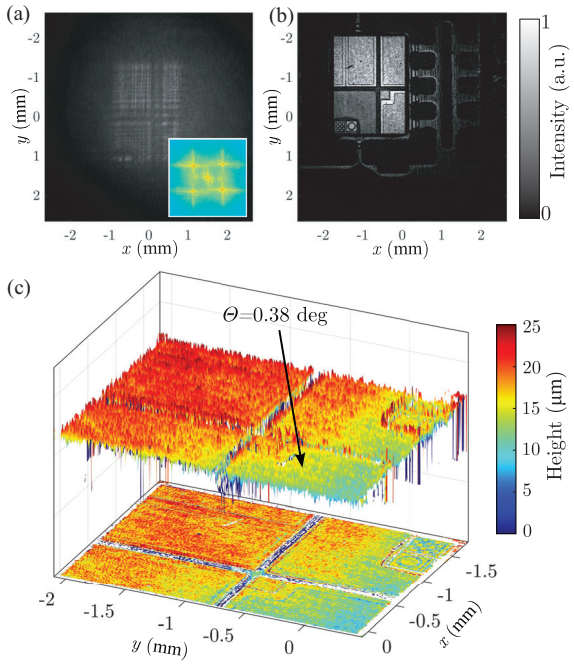

Fig. 6. DWDH application demonstration on chip tilt detection. (a) The captured dual-wavelength hologram and its spectrum. (b) Sum of the reconstructed intensities for λ_1 and λ_2. (c) Calculated height map and 3D topography map of the chip obtained from the beat phase. The tilt angle of the chip surface is indicated.

4. DISCUSSION

We demonstrated diffraction-limited lateral resolution DWDH. In the lensless configuration, the achievable resolution for two wavelengths using only a single detector and single frame acquisition is determined by the numerical aperture, but also by the correct choice of off-axis angle and pixel size Δx. The off-axis angle translates the spectrum of the sideband in the frequency domain, and the pixel size Δx determines the sensor bandwidth. Achieving the Abbe theoretical limit r_A is only possible when the sensor bandwidth covers the entire sideband. If the sideband surpasses the sensor bandwidth, which generally happens when the off-axis angle or system numerical aperture is too large, the achievable resolution will be worse than r_A. It is also worth mentioning that the spatial resolution in coherent imaging depends on the phase difference between two points [41]. Therefore, in real-world measurements of 3D objects, the achievable resolution can either be better or worse than the Abbe diffraction limit.

Although the DWDH FOV is given by the sensor size, in our experiment the useful FOV is more limited by the illumination beams that have a Gaussian light distribution that does not illuminate the entire FOV uniformly. To address this issue the illumination beam can be made more uniform with a flat-top beam collimator, which could be added after the beam expander.

Our paper investigates phase accuracy under conditions where shot noise is the dominant factor. For a polished mirror, the surface roughness is sufficiently small (less than 1 nm) so that decorrelation noise has very little influence. However, when the specimen has a rough surface, diffuse reflection can lead to speckle decorrelation, which deteriorates the phase measurement. Therefore, for phase accuracy measurements of rough objects, we recommend using the noise model proposed by Piniard *et al*. [37] along with the approach outlined in this paper to achieve a more precise prediction of phase accuracy.

The speed of the DWDH imaging proposed here is limited by two factors. First, the acquisition time of the camera, which typically ranged on the order of hundreds of microseconds, varying slightly depending on the reflectivity of the object. Notably, a single measurement proved sufficient to complete the entire imaging process. The imaging speed can be further enhanced by taking a higher-speed camera and more powerful light sources. Second, the data processing time is a few seconds for any of our experiments. We anticipate that faster data processing can be achieved with code optimization or conversion to a dedicated pre-compiled programming language.

In this paper, we only show one application case; nevertheless, we believe that this method will have multiple untapped industrial applications.

5. CONCLUSION

In this paper, we demonstrate a lensless single-shot DWDH system designed to address challenges encountered in modern industrial inspection. The dual-wavelength approach effectively extends the unambiguous measurement range to 50 μm in height. Combination off-axis and spatial frequency multiplexing offers a feasible solution for achieving single-shot dual-wavelength acquisition. We derive general expressions for quantifying and evaluating the phase accuracy for a DWDH setup from a single hologram under the condition of shot-noise-limited detection. Our experimental result shows a good agreement with our theoretical model. Also we demonstrate the capability of DWDH for 3D optical industrial inspection.

Funding. Nederlandse Organisatie voor Wetenschappelijk Onderzoek.

Disclosures. The authors declare no conflicts of interest.

Data availability. Data underlying the results presented in this paper are not publicly available at this time but may be obtained from the authors upon reasonable request.

REFERENCES

1. T. Yoshizawa, ed., *Handbook of Optical Metrology: Principles and Applications* (CRC Press, 2009).
2. R. Leach, ed., *Optical Measurement of Surface Topography* (Springer, 2011).
3. S. Catalucci, A. Thompson, S. Piano, *et al.*, "Optical metrology for digital manufacturing: a review," Int. J. Adv. Manuf. Technol. **120**, 4271–4290 (2022).
4. D. Gabor, "A new microscopic principle," Nature **161**, 777–778 (1948).
5. E. N. Leith and J. Upatnieks, "Reconstructed wavefronts and communication theory*," J. Opt. Soc. Am. **52**, 1123–1130 (1962).
6. E. Cuche, F. Bevilacqua, and C. Depeursinge, "Digital holography for quantitative phase-contrast imaging," Opt. Lett. **24**, 291–293 (1999).
7. B. Javidi, A. Carnicer, A. Anand, *et al.*, "Roadmap on digital holography [Invited]," Opt. Express **29**, 35078–35118 (2021).
8. W. Osten, A. Faridian, P. Gao, *et al.*, "Recent advances in digital holography [Invited]," Appl. Opt. **53**, G44–G63 (2014).
9. J. Zhang, S. Dai, C. Ma, *et al.*, "A review of common-path off-axis digital holography: towards high stable optical instrument manufacturing," Light Adv. Manuf. **2**, 333–349 (2021).

10. H. Zhou, M. M. R. Hussain, and P. P. Banerjee, "A review of the dual-wavelength technique for phase imaging and 3D topography," Light Adv. Manuf. **3**, 314–334 (2022).
11. J. van Rooij and J. Kalkman, "Sub-millimeter depth-resolved digital holography," Appl. Opt. **56**, 7286–7293 (2017).
12. D. Carl, M. Fratz, M. Pfeifer, *et al.*, "Multiwavelength digital holography with autocalibration of phase shifts and artificial wavelengths," Appl. Opt. **48**, H1–H8 (2009).
13. T. Colomb, S. Krivec, H. Hutter, *et al.*, "Digital holographic reflectometry," Opt. Express **18**, 3719–3731 (2010).
14. E. S. R. Fonseca, P. T. Fiadeiro, M. Pereira, *et al.*, "Comparative analysis of autofocus functions in digital in-line phase-shifting holography," Appl. Opt. **55**, 7663–7674 (2016).
15. M. A. Herráez, D. R. Burton, M. J. Lalor, *et al.*, "Fast two-dimensional phase-unwrapping algorithm based on sorting by reliability following a noncontinuous path," Appl. Opt. **41**, 7437–7444 (2002).
16. H. S. Abdul-Rahman, M. A. Gdeisat, D. R. Burton, *et al.*, "Fast and robust three-dimensional best path phase unwrapping algorithm," Appl. Opt. **46**, 6623–6635 (2007).
17. Z. Zhao, H. Zhang, Z. Xiao, *et al.*, "Robust 2D phase unwrapping algorithm based on the transport of intensity equation," Meas. Sci. Technol. **30**, 015201 (2018).
18. S. Park, Y. Kim, and I. Moon, "Automated phase unwrapping in digital holography with deep learning," Biomed. Opt. Express **12**, 7064–7081 (2021).
19. C. Wagner, W. Osten, and S. Seebacher, "Direct shape measurement by digital wavefront reconstruction and multi-wavelength contouring," Opt. Eng. **39**, 79–85 (2000).
20. J. Gass, A. Dakoff, and M. K. Kim, "Phase imaging without 2π ambiguity by multiwavelength digital holography," Opt. Lett. **28**, 1141–1143 (2003).
21. M. K. Kim, "Phase microscopy and surface profilometry by digital holography," Light Adv. Manuf. **3**, 481–492 (2022).
22. U. Abeywickrema, D. Beamer, P. Banerjee, *et al.*, "Holographic topography using acousto-optically generated large synthetic wavelengths," Proc. SPIE **9771**, 69–75 (2016).
23. X. Tian, X. Tu, J. Zhang, *et al.*, "Snapshot multi-wavelength interference microscope," Opt. Express **26**, 18279–18291 (2018).
24. M. T. Rinehart, N. T. Shaked, N. J. Jenness, *et al.*, "Simultaneous two-wavelength transmission quantitative phase microscopy with a color camera," Opt. Lett. **35**, 2612–2614 (2010).
25. J. Min, B. Yao, P. Gao, *et al.*, "Dual-wavelength slightly off-axis digital holographic microscopy," Appl. Opt. **51**, 191–196 (2012).
26. N. T. Shaked, V. Micó, M. Trusiak, *et al.*, "Off-axis digital holographic multiplexing for rapid wavefront acquisition and processing," Adv. Opt. Photonics **12**, 556–611 (2020).
27. M. Fratz, T. Beckmann, J. Anders, *et al.*, "Inline application of digital holography [Invited]," Appl. Opt. **58**, G120–G126 (2019).
28. M. Fratz, T. Seyler, A. Bertz, *et al.*, "Digital holography in production: an overview," Light Adv. Manuf. **2**, 283–295 (2021).
29. M. Piniard, B. Sorrente, G. Hug, *et al.*, "Melt pool monitoring in laser beam melting with two-wavelength holographic imaging," Light Adv. Manuf. **3**, 14–25 (2022).
30. J. Kühn, T. Colomb, F. Montfort, *et al.*, "Real-time dual-wavelength digital holographic microscopy with a single hologram acquisition," Opt. Express **15**, 7231–7242 (2007).
31. R. Guo and F. Wang, "Compact and stable real-time dual-wavelength digital holographic microscopy with a long-working distance objective," Opt. Express **25**, 24512–24520 (2017).
32. A. Khmaladze, M. Kim, and C.-M. Lo, "Phase imaging of cells by simultaneous dual-wavelength reflection digital holography," Opt. Express **16**, 10900–10911 (2008).
33. Z. Wang, Z. Jiang, and Y. Chen, "Single-shot dual-wavelength phase reconstruction in off-axis digital holography with polarization-multiplexing transmission," Appl. Opt. **55**, 6072–6078 (2016).
34. J. Kühn, F. Charrière, T. Colomb, *et al.*, "Axial sub-nanometer accuracy in digital holographic microscopy," Meas. Sci. Technol. **19**, 074007 (2008).
35. C. Remmersmann, S. Stürwald, B. Kemper, *et al.*, "Phase noise optimization in temporal phase-shifting digital holography with partial coherence light sources and its application in quantitative cell imaging," Appl. Opt. **48**, 1463–1472 (2009).
36. S. Chen and Y. Zhu, "Phase sensitivity evaluation and its application to phase shifting interferometry," Methods **136**, 50–59 (2018).
37. M. Piniard, B. Sorrente, G. Hug, *et al.*, "Modelling of the photometric balance for two-wavelength spatially multiplexed digital holography," Proc. SPIE **11783**, 1178308 (2021).
38. P. Hosseini, R. Zhou, Y.-H. Kim, *et al.*, "Pushing phase and amplitude sensitivity limits in interferometric microscopy," Opt. Lett. **41**, 1656–1659 (2016).
39. S. Chen, C. Li, C. Ma, *et al.*, "Phase sensitivity of off-axis digital holography," Opt. Lett. **43**, 4993–4996 (2018).
40. F. Charriére, B. Rappaz, J. Kühn, *et al.*, "Influence of shot noise on phase measurement accuracy in digital holographic microscopy," Opt. Express **15**, 8818–8831 (2007).
41. J. Goodman, *Introduction to Fourier Optics*, McGraw-Hill Physical and Quantum Electronics Series (W. H. Freeman, 2005).
42. L. J. van Vliet, D. Sudar, and I. T. Young, "Digital fluorescence imaging using cooled charge-coupled device array cameras," in *Cell Biology*, J. E. Celis, ed., 2nd ed. (Academic, 1998), Vol. **III**, pp. 109–120.